# An overpressure-time history model of methane-air explosion in tunnel-shape space

Di Chen[a], Chengqing Wu[a], Jun Li[a], Kexi Liao[b]

[a] *School of Civil and Environmental Engineering, University of Technology Sydney, Sydney, NSW, 2007, Australia*
[b] *Petroleum Engineering School, Southwest Petroleum University, Chengdu, Sichuan, 610500, China*

**Keywords**: CFD; methane-air explosion; tunnel-shape space; overpressure-time history model

**Abstract**

This study investigated methane-air explosion in tunnel-shape space and developed an overpressure-time history model based on numerical results. The findings revealed that for the progressively vented gas explosion with movable steel obstacles in a 20 m long tunnel, the inner peak overpressure increased as the activation pressure of the tunnel top cover got higher but less than 6 bar. However, as the activation pressure increased to eight bar or higher, the peak inner overpressure remained unchanged. As the segment cover panel became wider, the peak pressure was almost unchanged, but the pressure duration and impulse declined significantly. The peak pressure and impulse increased as the tunnel length vary from 10 to 30 m. With fixed tunnel length, higher blast pressure but lower impulse was observed as the inner obstacles were closer or the activation pressure of obstacles was higher. It is also found that a local enlarged space in the tunnel enhanced the peak pressure significantly. An overpressure time history model for the fixed tunnel top with enlarged end zone was established. The model considered activation pressure of vent cover, area and length of vent opening, methane concentration, number and blockage ratio of fixed obstacles was developed to calculate the overpressure and corresponding time at two characteristic points of the pressure-history curve. The cubic Hermite interpolation algorithm and a specially tuned formula consisting of the power and exponential function were used to interpolate pressure values between characteristic points. The proposed model can predict both the peak pressure and the overpressure time history with acceptable accuracy.

# 1 Introduction

Natural gas plays an increasingly important role in the global energy supply. In 2021, natural gas consumption surpassed 4 trillion cubic feet for the first time and accounted for nearly a quarter of the total energy demand globally (BP P.L.C, 2022). However, natural gas explosion is not uncommon and often results in tremendous casualties and economic losses (Chen et al., 2021). For example, 3934 gas explosion accidents with 4748 casualties occurred in China between 2016 and 2020 (Hu et al., 2022).

Gas explosions in tunnel-shape spaces, which have a large length-to-diameter (L/D) ratio, tend to develop much higher overpressure than explosions in unconfined spaces (Bjerketvedt et al., 1997). For example, as shown in Fig. 1, a destructive vapor explosion accident in Qingdao in 2013, which caused 62 deaths and 136 injuries, occurred in storm drains. The subsequent investigation revealed that the overpressure caused by the high degree of confinement (the drain) was so substantial that it damaged nearly 5 km drain reinforced concrete slab cover in sequential order and shattered the windows 100 m away from the epic center (Zhu et al., 2015). A maximum overpressure of 3.115 MPa was captured in a 1:5 scaled field test based on this explosion accident scenario, whose cover was assembled by 1 m wide concrete plates (Hou et al., 2021). Similarly, another gas explosion appeared in an underground trench in Kaohsiung in 2014, which caused 32 deaths and 321 injuries, blew out about 400 m long road surface (Fig. 2), and cracked longer (Yang et al., 2016). The two accidents above, categorized as progressive vented gas explosions (Chen et al., 2022), happened in tunnel-shape spaces where the length over cross-section size ratio is very large, provided the combustion process with enough long space to boost the overpressure.



Fig. 1 The explosion site in Qingdao (Hou et al., 2021)



Fig. 2 The explosion site in Kaohsiung (Hou et al., 2021)

Gas explosion in tunnel-shape space has been widely studied experimentally and numerically. Zhao et al. (Zhao et al., 2022) investigated the effects of length and vent conditions on load characteristics in utility tunnels in a steel chamber with a cross-section size of 140 ×160 mm. Two cylindrical ports at both ends of the compartment model,

which are a common practice to act as entrance or exit for maintenance, escape, ventilation, etc., were used as the vent opening. It was observed that the vent opening at the far end of the enclosure led to much higher overpressure (~45% increase) as compared to that of the vent opening located at the ignition side, and the peak pressure for the far end vent opening explosion was close to the peak pressure that captured in the chamber with no venting (0.395 MPa VS 0.401 MPa). Yang et al. (Yang et al., 2022) studied the effect of vent location and methane concentration on pressure load characteristics in a 30 m long steel tube with a square section of $0.8 \times 0.8$ m and concluded that the existence of vents attenuated the overpressure and impulse efficiently. The CFD code FLACS was verified and then used to supplement the test results. Zipf et al. (Zipf et al., 2013) investigated the methane-air detonation process in a steel tube with a 73 m length, 105 cm internal diameter and internal obstacles, and a maximum shock pressure of 1.7 MPa was captured.

Generally, the container wall in the abovementioned maintained integrity during explosion process. However, catastrophic destruction of the drain/trench cover was observed in the accident in Qingdao and Kaohsiung (Hou et al., 2021). The large deformation of the cover changed the tunnel's confinement level, influencing the load characteristics. Some recent experiments have considered the effect of tunnel cover deformation. Meng et al. (Meng et al., 2020a; Meng et al., 2020b; Meng et al., 2021) conducted a series of experiments in a 20 m long utility tunnel, in which steel slabs acting as the tunnel cover were lifted one by one in the explosion process. Another similar experiment, conducted in an 80-meter-long utility tunnel, also captured the sequential lifting of tunnel cover (Hou et al., 2021). A numerical model, considering the sequential lifting of tunnel cover, termed a progressive vented gas explosion, was established and validated by Chen et al. (Chen et al., 2022).

Although gas explosion load can be obtained accurately by experimental studies, it is not always accessible for engineering protection design practice because large-scale gas explosion tests are often prohibitive due to the high cost and safety issues. Owing to its capability and accuracy in handling large-scale gas explosion scenarios (hundreds of meters), FLACS is widely used in the study of gas explosions in the engineering-scale tunnel (Li et al., 2020; Lin et al., 2022; Zhang et al., 2020; Zhu et al., 2021; Zhu et al., 2020). However, such refined numerical simulations are often computationally expensive and time-consuming. Therefore, researchers have developed some empirical/semi-empirical models using experimental and numerical data. The US standard provides a formula considering the vent size and vent opening pressure to calculate the maximum overpressure for design purposes (National Fire Protection Association, 2023). Moreover, the European standard BS EN 14994 provides a model to calculate the gas overpressure

with venting in an individual room (European Committee for Standardization, 2007). More models can be found in the literature to estimate the peak pressure for gas explosion (Bradley and Mitcheson, 1978a, 1978b; Canu et al., 1990; Chippett, 1984). However, these models aim at prediction on the peak overpressure rather than accurate overpressure-time history curve, and the latter is required for assessing the dynamic structural response. Recently, an empirical overpressure-history model was developed to calculate the methane-air explosion load in a room-shape space where the dimensions of length, height, and width are comparable (Yang et al., 2021). Still, no similar model was found for the load in tunnel-shape space. Usually, the inside load is evenly distributed for room-shape spaces (Li et al., 2017). However, as the flame accelerates, the load develops along the tunnel length in a tunnel-shape space, hence is unevenly distributed.

This study compares the load characteristics of methane-air explosion in tunnel-shape structure with different boundary conditions. First, a parametric study about the vent cover strength and width, tunnel length, obstacles' distance and activation pressure, and the dimensions and position of local space expansion was carried out to explore the load characteristics. Then, an overpressure-history model was proposed and validated based on the simulation dataset. The results of this study provide some references for the explosion load determination and blast resistant design of tunnel-shape space, hence helping mitigate the impact of gas explosion disasters.

## 2 Numerical model and verification

Two types of tunnel chambers, i.e., total-confined and progressively venting gas explosions are considered. For the progressively vented gas explosion, the tunnel top cover plates were lifted progressively by the internal gas explosion overpressure. While for the total-confined scenario, the tunnel top was rigid with/without vent opening. The CFD code, FLACS, was utilized to simulate the two types of gas explosion. This widely validated tool was specially tuned to simulate gas explosions in realistic industrial geometries (Gexcon, 2019). As illustrated in Fig. 3, the CFD result of the progressive vented methane-air explosion was validated in the previous work (Chen et al., 2022).
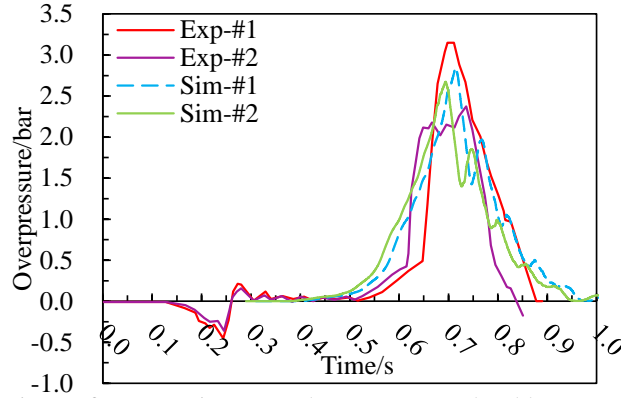
**Fig. 3** The comparison of progressive vented overpressure load between the numerical and experimental results (Chen et al., 2022)

A further validation was performed on a methane-air explosion in a total-confined tunnel-shape space, and the CFD result was validated against the experimental data reported by Li et al. (Li et al., 2021). As shown in Fig. 4, the experimental apparatus consisted of a 30 m long tube with a square cross-section of $0.8 \times 0.8$ m, and both ends of the tube were closed. Ten sections with a length of 3 m were used to assemble this long tube. The 1st section (3 m) was filled with a 9.5% methane-air mixture, and the ignition position was located at the section center of one end. The pressure sensor was installed at one-third of each section. This experimental scenario was reproduced by FLACS, and the pressure history curves were compared.
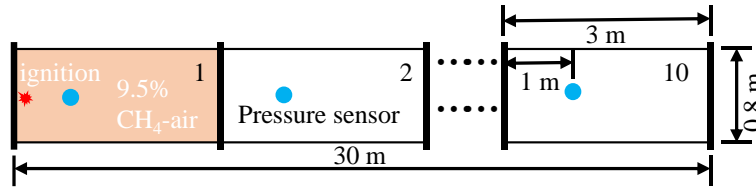


**Fig. 4.** Schematic diagram of the total-confined methane-air explosion experiment (Li et al., 2021)

Two overpressure time history curves captured at the two ends of the tube are compared in Fig. 5. The first pressure peak and the pressure increasing trend captured from the CFD model and experiment approximately coincided with each other. It can also be observed that the pressure was oscillating in the tube, and the oscillation period from the simulation agreed well with the experimental results. However, after the fuel finished combustion and the pressure wave started to oscillate in the tube, the pressure attenuation from the numerical model was slower than the experimental results. This may result from either the heat loss model in the FLACS which is not suitable for such a long period of time (usually the heat loss is negligible for the explosion process) or the imperfect sealing performance of the experimental tube, as it was assembled by flanges; hence some leakage might occur when the internal pressure was high which would accelerate the pressure decreasing. The peak pressure at the monitoring points in the tube is listed in Table 1. The maximum relative error between the numerical and experimental results was

within 20% which indicates FLACS can yield respectable accuracy in the total-confined tunnel-shape space.
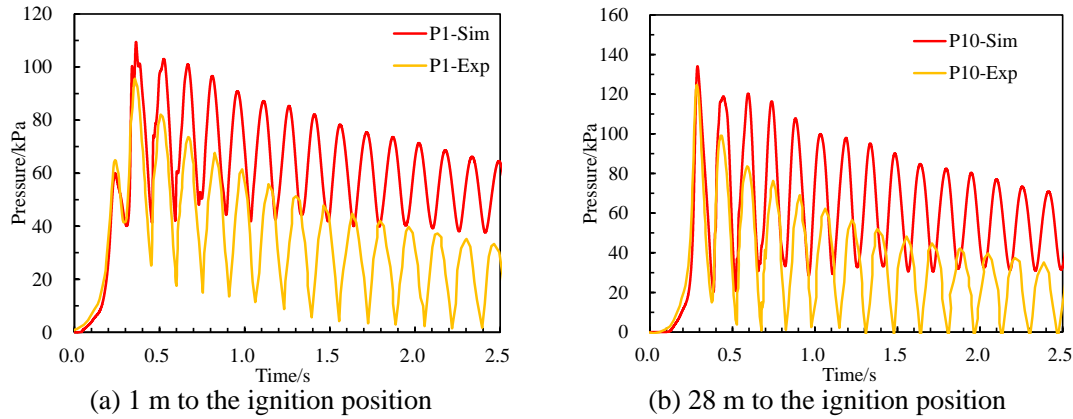


(a) 1 m to the ignition position　　　　(b) 28 m to the ignition position

**Fig. 5.** Overpressure history comparison (Li et al., 2021)

**Table 1** Peak pressure comparison of the experimental and numerical results (Li et al., 2021)

| Distance/m | Numerical pressure/kPa | Experimental pressure/kPa | Relative error |
|---|---|---|---|
| 1 | 60.0 | 61.1 | -1.8% |
| 7 | 61.7 | 57.6 | 7.1% |
| 10 | 69.8 | 60.6 | 15.1% |
| 16 | 66.5 | 66.5 | 0.0% |
| 19 | 68.6 | 72.6 | -5.5% |
| 22 | 112.5 | 95.5 | 17.8% |
| 28 | 134.1 | 115.4 | 16.2% |

## 3 Parametric study of tunnel's boundary condition on load characteristics

A parametric study was performed to investigate the effect of vent cover conditions, tunnel length, inner obstacles, and local expansion on explosion overpressure and impulse.

### 3.1 Physical model

Two types of tunnel-shape chambers were studied to observe the difference in blast pressure time histories. One was that the tunnel cover was considered as rigid, while the other was regarded as progressive vented. Both ends of the chamber were closed to simulate the utility layout to control the accident range as required by Chinese standard GB 50838-2015 (Ministry of Housing and Development, 2015). In the parametric study, the cross-section was rectangular with dimensions of 1.6 m wide and 0.6 m high, while tunnel length was a variable parameter, with values of 10, 20, and 30 m. Other variables include the activation pressure and the vent panel width of the tunnel cover, the distance and the activation pressure of internal obstacles. The local expansion at the tunnel end was established to model the entrance and exit for escape, ventilation, equipment lifting, etc. The dimensions of local expansion and the relative positions were compared in this study. According to literature (Lin et al., 2020; Liao et al., 2023), the buried depth of the utility tunnel varied from 0.5 to 4.5 m after counting more than 700 km long tunnels in China. More specifically, the manholes with a height of about 2 m account for 80% of the

254 investigated manholes (Li et al., 2019). In this study, the local expansion heights of 0.6, 1.2 and 2.4 m were considered, so the simulation results would cover the most common scenarios. With a worst-consequence basis, the tunnel was filled with a homogeneous methane-air mixture with a stoichiometric ratio of 1.1, and the ignition point was placed at the center of one end of the tunnel (Puttock et al., 2000).

## 3.2 Numerical model

### 3.2.1 Numerical domain and mesh

As validated in the literature (Chen et al., 2022), a cubic grid with the size of 5 cm was sufficiently small for the fuel region, and the numerical domain was stretched enough to avoid boundary effect and allow for proper resolution of external explosion (Gexcon, 2019).

### 3.2.2 Boundary conditions

The tunnel wall was modeled as rigid. The thermal effect between the hot fluid and the tunnel wall was considered. Specifically, the thermal convection was activated by setting the parameter, *heat_switch*, to 1, while the command line, *KEYS = " RADIATE=04"*, was utilized to specify the heat by radiation. The Wall function was activated to resolve the effect of momentum boundary layers near the wall regions. As for the computational domain boundary, the EULER boundary was set in the ground direction to mimic the reflective effect. The other five boundaries were defined as PLANE_WAVE to reduce the reflection of pressure waves at the boundaries.

### 3.2.3 Initial conditions

As recommended by the FLACS user's manual (Gexcon, 2019), initial conditions for gravity, turbulence intensity, initial temperature and pressure, air components, and ignition condition are summarized in Table 2.

**Table 2** Initial conditions for the numerical model

| Parameter | Value |
|---|---|
| Gravity | 9.8 m/s$^2$ |
| Characteristic velocity | 0 m/s |
| Relative turbulence intensity | 0 |
| Turbulence length scale | 0 m/s |
| Temperature | 20℃ |
| Ambient pressure | 1 bar |
| Air composition | 20.95 % $O_2$+79.05 % $N_2$ |
| Ignition time | 0 s |
| Dimension of ignition | 0 m$^3$ (point ignition) |

### 3.2.4 Monitor point position

Monitor point was used to record the variables in the computational domain, such as overpressure and impulse, during the simulation process. Fig. 6 illustrates the relative position of monitor points in the tunnel: they were distributed at the center of the tunnel's cross-section along the tunnel length from the ignition to the opposite end with a distance of 1 m.
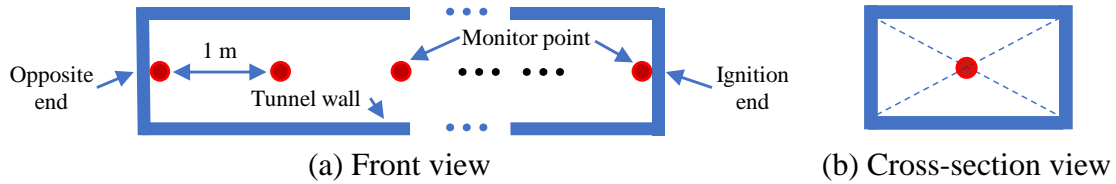


(a) Front view        (b) Cross-section view

**Fig. 6.** Relative position of monitor point

## 3.3 Vent cover conditions

### 3.3.1 The activation pressure

The geometry model is shown in Fig. 7. The inner dimensions of the tunnel were 20 m long, 1.6 m wide, and 0.6 m deep. Twenty-one monitor points were placed at the center of the tunnel cross-section from 0 m to 20 m with a pace of 1 m to track the history of overpressure and impulse. Nineteen pressure relief panels were placed in the tunnel with an activation pressure of 0.006 bar to act as movable steel obstacles, as described in the literature (Chen et al., 2022). The vent cover consisted of 50 vent panels each with a width of 0.4 m. The activation pressures of the vent cover were set as 2, 4, 6, 8, and 10 bar, respectively, to simulate the progressive venting.
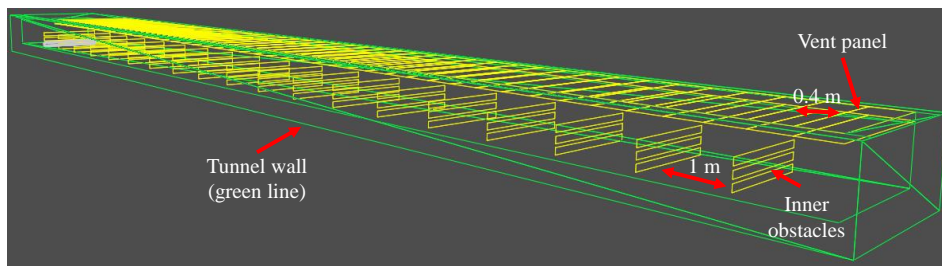


**Fig. 7.** The geometry model

The overpressure time history curves at the opposite tunnel end of the ignition point are illustrated in Fig. 8 (the same position in the rest of Section 4). The maximum pressure peak was 2.85 bar when the vent activation pressure was two bar, and it climbed to 6.28 bar as the activation pressure was six bar. However, when the activation pressure reached eight bar or higher, the vent cover could not be lifted, and the tunnel remained a total-confined space during the whole explosion process (constant volume explosion). As a result, the maximum overpressure was 7.52 bar for the cases of 8 and 10 bar vent activation pressure. Methane-air mixture explosion at the initial conditions of 25 ℃ and 1 bar resulted in a peak pressure of 7.94 bar for constant volume explosion (Bjerketvedt

et al., 1997), which explained why the peak overpressure did not increase as the activation pressure of vent cover reached 6 bar or higher.
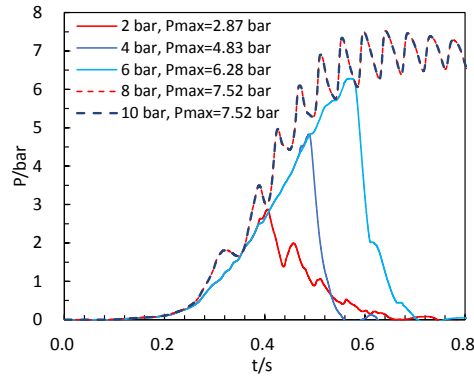


**Fig. 8.** The pressure history curves with different activation pressures

### 3.3.2 The width of vent openings

The tunnel dimensions and the inner obstacles were in line with those in section 4.1.1. The vent openings with the single vent panel width of 0.4, 0.8, 1.67, 2.22, and 4 m were considered so that the vent cover would consist of 50, 25, 12, 9, and 5 panels. The activation pressure was set as two bar.

The pressure history (Fig. 9 a) and maximum impulse along the tunnel length (Fig. 9 b) are depicted in Fig. 9. The overpressure peaks did not show distinct differences and were close to 2.85 bar. However, the pressure duration declined visibly as the single vent panel width increased from 0.4 to 0.8 m, and it experienced a minor decrease as the vent panel width increased further. As for the impulse, generally, the maximum impulse was lower when the vent panel was wider. The maximum impulse increased as the distance from the ignition point increased in each case. Therefore, it can be concluded that wider vent panels tend to cause less severe consequences.
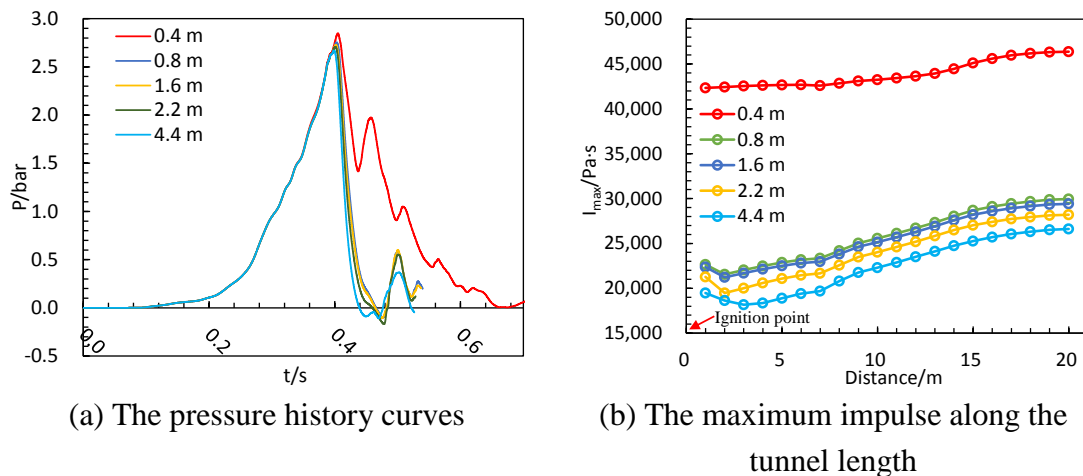


(a) The pressure history curves

(b) The maximum impulse along the tunnel length

**Fig. 9.** The effect of vent opening width

## 3.4 Tunnel length

The effect of tunnel length on explosion overpressure and impulse was investigated in this study. The tunnel lengths of 10, 20, and 30 m were considered, while the 1.6 m wide and 0.6 m deep tunnel cross-section, which was the same as that in section 4.1, were chosen for exploration. The inner obstacles' activation pressure was 0.006 bar. Thirty groups of internal obstacles were selected for each case, meaning the spacing of obstacles was 0.33, 0.67, and 1.00 m, respectively, for the 10, 20, and 30 m long tunnel. The 0.4 m wide vent panels with an activation pressure of 2 bar were utilized to compose a progressive vented tunnel cover.

Fig. 10 presents the pressure profiles influenced by tunnel length. The maximum overpressure was 2.64 bar in the 10 m long tunnel, increasing to 4.22 bar in the 20 m long tunnel and 5.04 bar in the 30 m long tunnel. Meanwhile, the positive load durations were about 310 ms, 350 ms, and 395 ms, respectively. Moreover, two prominent pressure peaks can be observed from the load profile, although the second peak for the 10 m long tunnel was less pronounced. The backflow phenomenon and flame acceleration can explain the reason for the occurrence of the second peak. Fig. 11 presents the flame development in the 20 m long tunnel. The acceleration of flame in the tunnel increased the overpressure continuously before it exceeded the activation pressure of the tunnel cover, and the overpressure reached its first peak at the start of venting (Fig. 11 a). As shown in Fig. 11 b, the overpressure started to drop as the vent opening efficiently discharged the burnt gas at 0.297 s. In addition, the flame front moved towards the vent opening, resulting in a backflow phenomenon. This sort of backflow phenomenon impeded the flow of flame to the unburned methane-air mixture, hence reducing the combustion rate, which was also observed in a progressive vented gas explosion test in an 80 m long tunnel (Hou et al., 2021). It should be noted that the combustion process did not stopped, and there was still around 6.0 m long of unburned fuel at the left side of the tunnel, although the combination of the venting and backflow phenomenon led to the overpressure drop. Ten milliseconds later, as presented in Fig. 11 c, the flame length started to increase again, indicating that the influence of combustion overcame the effect of the venting and backflow phenomenon. Therefore, the overpressure began to grow and reached its second peak. The second pressure peak was less significant in the 10 m long tunnel as there was a much shorter length of unburned fuel (about 2.2 m as shown in Fig. 12) when the venting process was initiated, so not enough fuel could be burnt to overcome the effect of venting and backflow phenomenon.
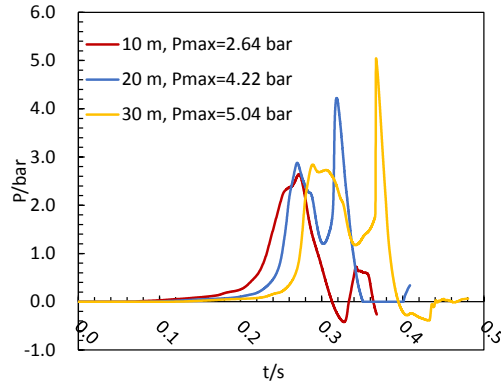
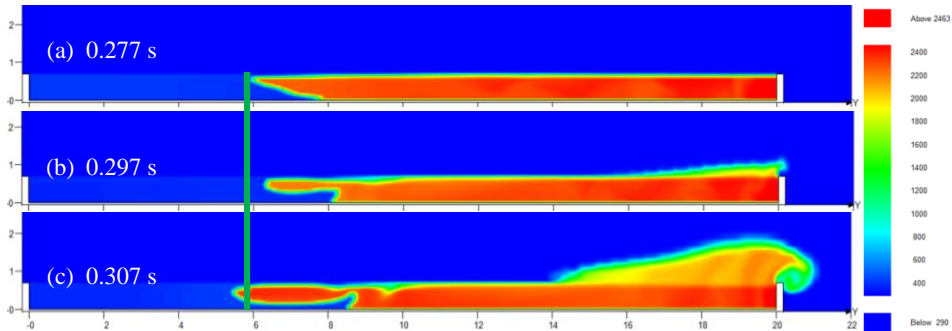**Fig. 10.** The pressure history curves with different tunnel length



**Fig. 11.** The temperature contour before, at the beginning of, and after venting in the 20 m long tunnel
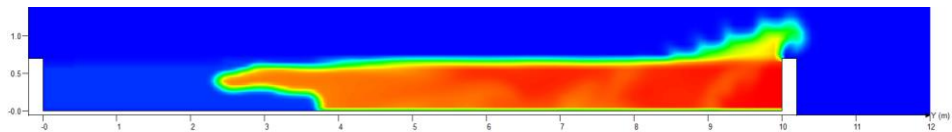


**Fig. 12.** The temperature contour at the beginning of venting in the 10 m long tunnel

The maximum overpressure and impulse along the tunnel are presented in Fig. 13. Generally, longer tunnels produced higher peak pressure and impulse, and the maximum overpressure and impulse increased from the ignition to the opposite end in each length of the tunnel. However, the increasing trend was not consistent along the tunnel length direction in each case, resulting from the different dominant factors of venting, backflow phenomenon, and flame acceleration.
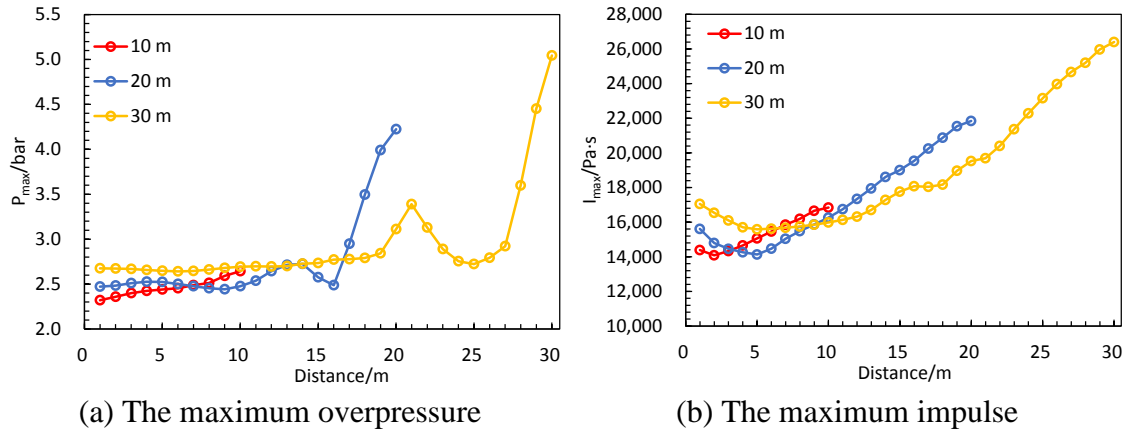


(a) The maximum overpressure

(b) The maximum impulse

11

## 3.5 Inner obstacles

The presence of obstacles provides the flow field extra turbulence, accelerating the combustion rate and significantly enhancing the overpressure. This section investigated the effect of obstacle separation distance and activation pressure. The tunnel dimensions were 20 m long, 1.6 m wide, and 0.6 m deep. A progressive vented tunnel cover that was the same as in section 4.1 was utilized.

3.5.1 The separation distance between obstacles

The obstacle separations of 1, 0.75, and 0.25 m with the activation of 0.006 bar represented the movable obstacles. As shown in Fig. 14, closer obstacles caused higher overpressure and shorter pressure duration. The maximum overpressure of 4.22 bar was captured when the separation distance was 1 m. As the distance of obstacle separation decreased to 0.25 m, the peak pressure increased significantly and reached 8.51 bar. However, the positive load duration declined as the obstacles got closer, which reduced from about 350 ms to 280 ms when the obstacle distance varied from 1 m to 0.25 m. The number of dominant pressure peaks was two when the separation was 1 m and 0.75 m, while it declined to one when the obstacle distance was 0.25 m. Again, this can be explained by the lack of fuel to support the second flame acceleration and overcome the influence of venting and backflow, because a large portion of the methane-air mixture was consumed before the inception of venting due to the stronger turbulence caused by the closer obstacles.
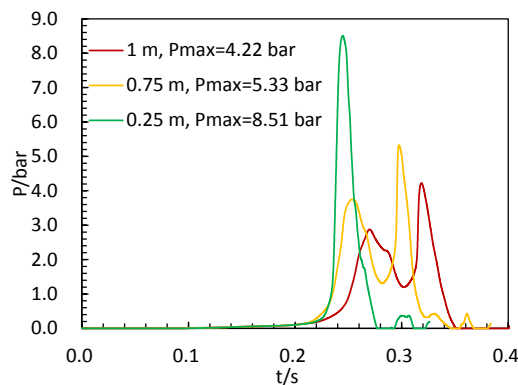


**Fig. 14.** The pressure history curves with obstacle distances of 1 m, 0.75 m, and 0.25 m

Fig. 15 illustrates the maximum overpressure and impulse along the tunnel. The primary trend was that the maximum overpressure and impulse increased as the monitor point got farther from the ignition end for each case of obstacle distance. At the same distance from the ignition end, the closer the obstacle distance was, the higher peak pressure and

impulse were. Clear inflection points were observed in Fig. 15 (a), as the maximum pressure soared rapidly when the monitor points closed to the opposite of the tunnel. This was explained by the reflection of pressure wave at the tunnel end. The reflected pressure will typically increase by a factor of 2 as compared to incident pressure for gas explosion, and higher-pressure strength will lead to more notable increase (Bjerketvedt et al., 1997). Such an inflection point can also be noted at the ignition end in the case of 0.25 m separation distance of obstacles. However, the other two cases have not shown such inflection point at the ignition end. This difference was caused by the different pressure rising rates. As shown in Fig. 14, the overpressure rose in a much more rapid rate for the case of 0.25 m separation distance as compared to the other two cases. Therefore, prior to the completion of venting, the overpressure continued rising and the reflected pressure wave transmitted from the opposite end to the ignition end and caused the inflection point at the ignition end. By comparison, for the cases of 0.75 and 1 m separation distance, their pressure rising rates were much slower. Before the tunnel covered finished its venting, the overpressure in the tunnel was released sufficiently, so when the reflected pressure wave transmitted to the ignition end, the pressure strength was so weak that no inflection point was caused.
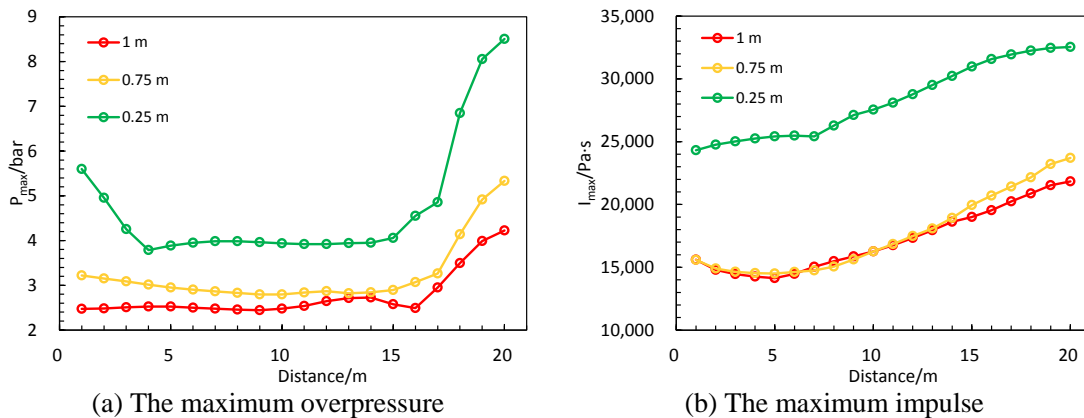


(a) The maximum overpressure        (b) The maximum impulse

**Fig. 15.** The maximum overpressure and impulse distribution along the tunnel with obstacle distances of 1 m, 0.75 m, 0.5 m, and 0.25 m

### 3.5.2 The activation pressure of obstacles

The influence of the activation pressure of obstacles was explored in this section. The 1 m distance of obstacles with the activation pressure of 0.006, 0.012, 0.024, 0.036,' 0.048, 0.06 bar was considered. One simulation with fixed obstacles was also considered (the activation pressure was 999 bar so the obstacles will never fail during the whole explosion process). Other conditions were identical to that in section 3.5.1. As shown in Fig. 16, higher activation pressures resulted in higher peak pressure but shorter load duration. The peak pressure of 4.22 bar was captured when the activation pressure was 0.006 bar, while it soared to 20.23 bar when the obstacles were fixed in the tunnel bottom. The reason was that higher activation pressure could prolong the existence of obstacles in the tunnel.

Hence more turbulence can be provided in the combustion process, and the overpressure was boosted. However, the load duration was shortened due to the stronger obstacles because the combustion rate was enhanced, but the total amount of fuel in each case was identical.
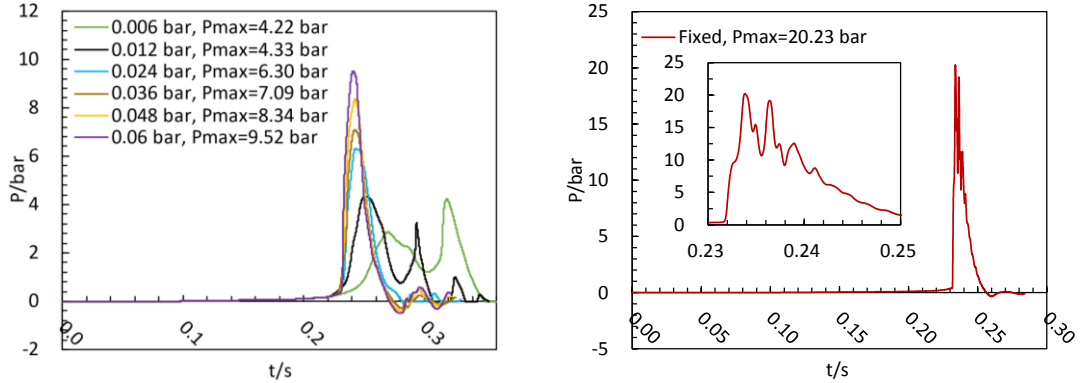


**Fig. 16.** The pressure history curves with obstacle activation pressure of 0.006, 0.012, 0.024, 0.048, 0.06 bar and fixed obstacles

As illustrated in Fig. 17 (a), the maximum peak pressure variation trend was similar to section 4.3.1. Still, the maximum impulse presented a distinct difference, as shown in Fig. 17 (b). In general, those which had higher peak pressures gave lower impulses. At the ignition end, the maximum impulse was close to 8400 Pa.s when the obstacles were fixed. By comparison, the values increased by almost a half and were about $1.5 \times 10^4$ Pa.s when the activation pressure was 0.006 bar.



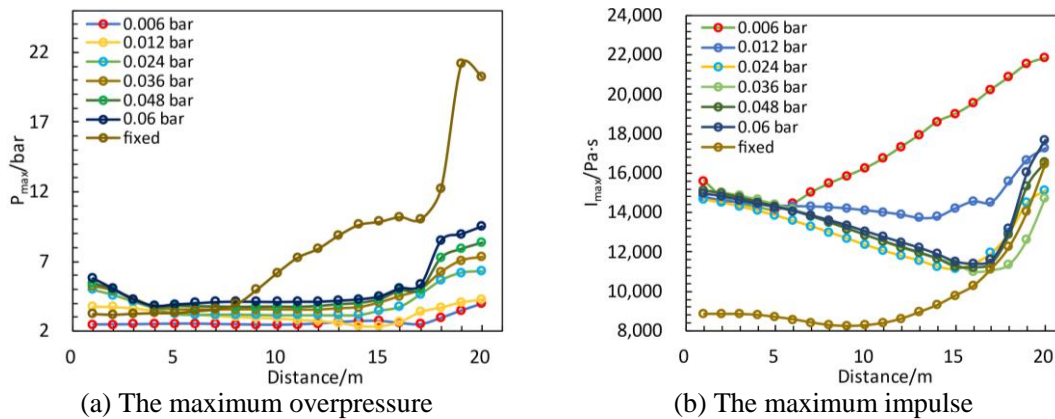(a) The maximum overpressure          (b) The maximum impulse

**Fig. 17.** The maximum overpressure and impulse distribution along the tunnel with obstacle activation pressure of 1, 2, 4, 8, 10 times and fixed obstacles

## 3.6 Local expansion along the tunnel length

The local cuboid expansion along the tunnel length was established to model the entrance and exit in the tunnel. The expansion was modeled by rigid walls to present the most severe scenarios (shown in Fig 18). The tunnel was 20 m long, 1.6 m wide, and 0.6 m deep. Pressure relief panels modeled the tunnel cover with a width of 0.4 m and activation of two bar. Inner obstacles with a distance of 1 m and activation pressure of 0.006 bar were placed at the bottom of the tunnel. The effects of expansion dimension and relative

position were investigated. The local expansion was filled with air (no methane) to maintain the same amount of fuel.
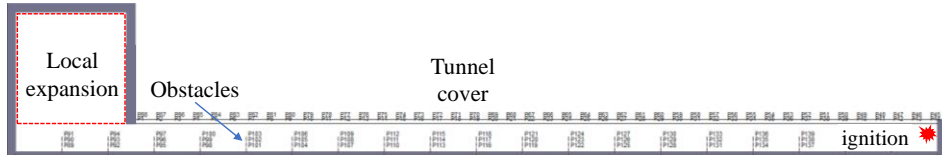

Fig. 18 Geometry model of the tunnel with local expansion.

3.6.1 Dimensions of the expansion

The dimension of local expansion was studied. Cuboid expansions with the dimensions of 0.6 (width)×0.6 (height) m, 0.6×1.2 m, 1.2×1.2 m, 1.2×2.4 m, and 2.4×2.4 m were established at the tunnel end far away from the ignition end. The load captured from the tunnel with no expansion was also compared. As shown in Fig .19 and Fig. 20, no distinct differences were observed as compared to the case with no expansion when the expansion size was small (1.2×1.2 m or smaller). The peak pressure decreased from 4.22 bar to 3.30 bar, and the load duration increased slowly as the expansion size rose from zero to 1.2×1.2 m, then the peak pressure soared to 6.75 bar as the dimensions of expansion reached 1.2×2.4 m; as the dimensions of expansion increased further, the peak pressure increased slightly to 6.88 bar. As shown in Fig. 20 (a) the peak pressure increased as the distance between the ignition point and monitor location increased. The maximum overpressure encountered a noticeable drop near the expansion but increased again in the case of 2.4×2.4 m expansion. As shown in Fig. 20 (b), the magnitude of impulses was quite close along the tunnel length before the dimension of expansion reached 1.2×1.2 m, but soared dramatically from round $2.0×10^4$ Pa.s to more than $3.0×10^4$ Pa.s from the ignition to the opposite end of the tunnel as the expansion increased to 1.2×1.2 m or bigger.


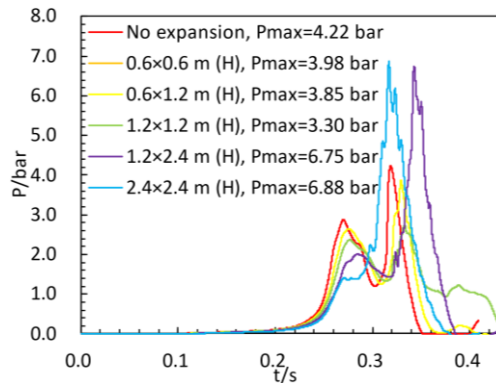**Fig. 19.** The effect of cuboid dimensions on pressure history curves

15

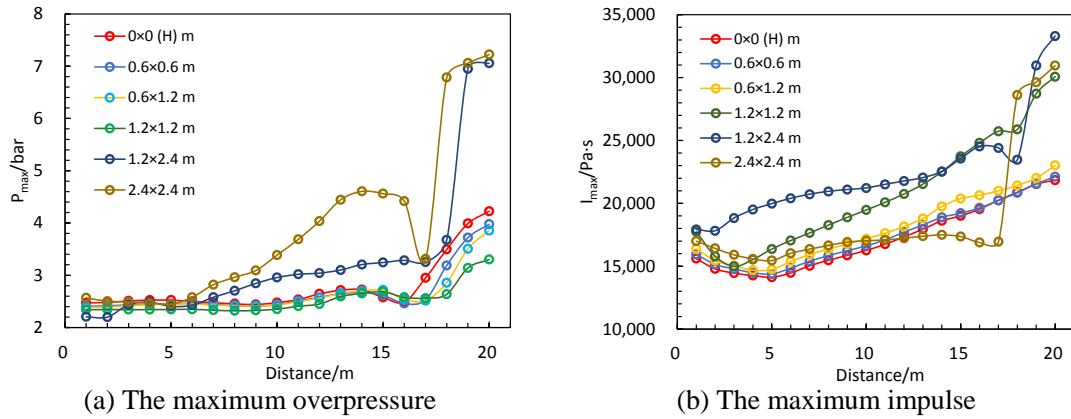|  (a) The maximum overpressure  |  (b) The maximum impulse  |

**Fig. 20.** The maximum overpressure and impulse distribution along the tunnel with different cuboid expansion dimensions

The underlying mechanisms of the effect of local expansion on the explosion load were explained as follows. Firstly, the local expansion functioned as a cage to trap the pressure waves, which would enhance the load. The pressure wave reflected repeatedly in the expansion instead of propagating out of the tunnel through the vent opening. Hence less pressure can be leaked to the surroundings. Here this phenomenon was named as "cage effect". Secondly, the local expansion also provided extra space for the burned/unburned gas in the tunnel to expand before the tunnel cover started to fail (Fig. 21 b), leading to a weaker load. This was called the "expansion effect" here. After that, extra turbulence was provided by the local expansion as a sudden change occurred in the tunnel, which would boost the load in the tunnel and was called the "turbulence effect". As illustrated in Fig. 21, a distinct vortex driven by the pressure wave can be observed near the expansion, and the fuel was pushed into the expansion and mixed with air. In addition, the kinetic energy (presented by velocity) was converted to potential energy (delivered by overpressure) when the burned/unburned gas flowed from a narrow path (tunnel) to a broader path (expansion), which would lead to higher explosion pressure and was controlled by Bernoulli effect (Feldgun et al., 2011). As illustrated in Fig. 22, the velocity magnitude dropped dramatically as the fluid reached the expansion. Three monitor points of pressures and velocities were compared at 16, 17, and 18 m from the ignition point. From most minor to most significant, the velocity ranking was v-18 m, v-16 m, and v-17 m. On the contrary, the pressure ranking was P-17 m, P-16 m, and P-18 m. Finally, the expansion helped to increase the contact region between the flame and the fuel as the expansion had a more extensive cross-section, which would contribute to a higher explosion load and was named as jet flame effect as described in the literature (Bjerketvedt et al., 1997). Those five factors had different degrees of influence on each size of the expansion. The expansion and Bernoulli effects dominated the load development when the expansion size was small. By comparison, the cage, turbulence, and jet flame effects controlled the increase in explosion pressure as the dimension of expansion reached a certain magnitude.
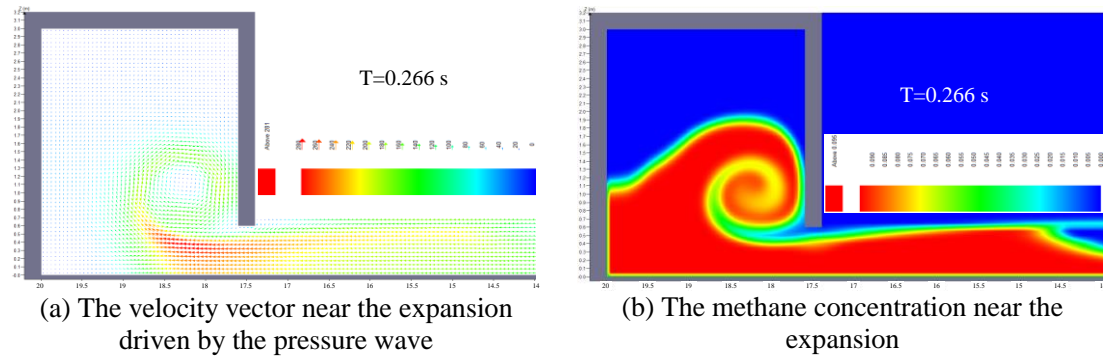
(a) The velocity vector near the expansion driven by the pressure wave



(b) The methane concentration near the expansion

**Fig. 21.** The "turbulence effect" caused by the 2.4×2.4 m expansion



(a) The pressure history curves near the expansion (the expansion is from 17.5 m to 20.0 m)



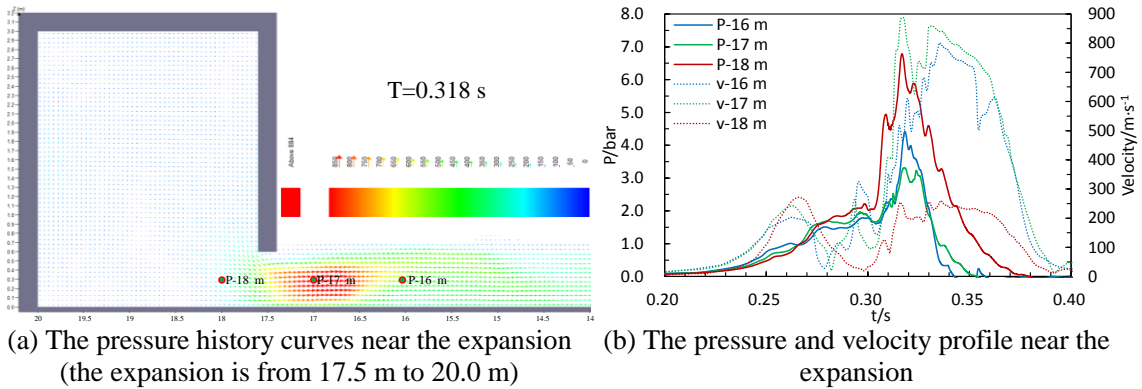(b) The pressure and velocity profile near the expansion

**Fig. 22.** The Bernoulli effect caused by the 2.4×2.4 m expansion

### 3.6.2 The relative position of expansion

The expansion positions at the ignition end, one-fourth tunnel length away from the ignition end, 2/4 tunnel length away from the ignition end, 3/4 tunnel length away from the ignition end, and 4/4 tunnel length away from the ignition end were investigated. The expansion size was 2.4×2.4 m, while the other boundary conditions were the same as in section 4.4.1. It was found that the maximum overpressure was close to that of no expansion tunnel when the expansion was located at the ignition end and the one-fourth tunnel length away from the ignition end. However, the load duration for the case where the expansion was situated in the ignition was more prolonged than in other cases and was almost 500 ms. This was due to the expansion effect that the ignition position was just right in the local expansion, so extra expansion space was provided for the burned gas when the explosion process was initiated, which reduced the confined level of the tunnel notably and slowed the combustion process and decayed the acceleration of flame. It should be noted that although the lowest pressure was observed when the local expansion was at the ignition end, the impulse was almost kept the highest along the tunnel length except when monitor points were closed to the opposite side of the ignition end, as shown in Fig. 24 (b). A significant increase in peak pressures was captured as the local expansion moved to the middle of the tunnel or farther away from the ignition end. The maximum pressure of 7.79 bar was observed when the expansion was located at the

middle of the tunnel, but the impulse was the lowest as the pressure duration was shorter than in other cases. The maximum pressure for the case where the expansion was located at the opposite end away from the ignition side was only 0.27 bar lower than the middle expansion case, but it had the highest impulse. So, the consequences of gas explosion tend to be the most severe when the expansion is at the opposite end away from the ignition side by considering the peak pressure and impulse together. It can be concluded that the effect of the relative position of local expansion was quite complex, as there was no monotone variation trend when the expansion location changed along the tunnel length monotonically, and it was not necessary to reach the highest impulse when the load duration was the longest, nor the highest overpressure when the impulse was the greatest.
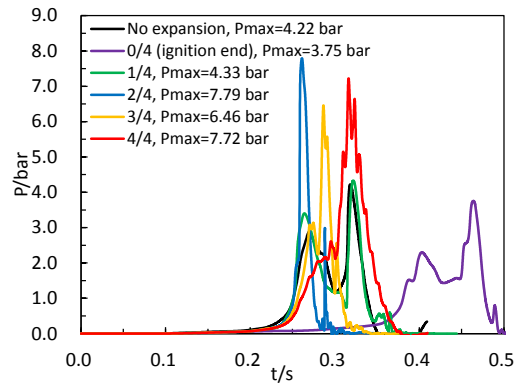


**Fig. 23** The pressure history curves with no expansion and expansion at the 0/4 (ignition end), 1/4, 2/4, 3/4, and 4/4 of the tunnel length



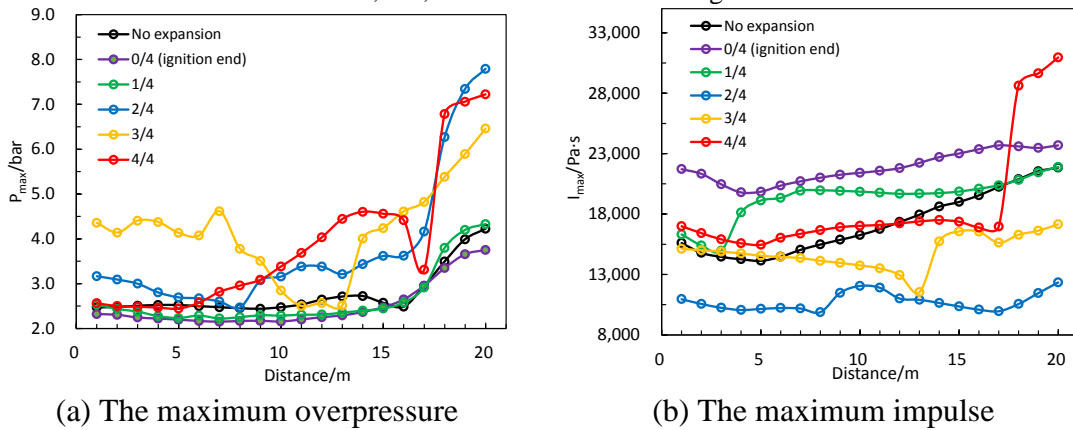(a) The maximum overpressure       (b) The maximum impulse

**Fig. 24.** The maximum overpressure and impulse distribution along the tunnel with no expansion and expansion at the 0/4 (ignition end), 1/4, 2/4, 3/4, 4/4 of the tunnel length

## 4 Overpressure-history prediction model

The effects of vent cover conditions, tunnel length, inner obstacles, and local expansion on methane-air explosion loads were investigated in the previous section. It is found that the consequence tends to be the most severe when the tunnel cover was rigid, the obstacles were fixed, and the local expansion was at the far end of the tunnel. The derivation of the overpressure-history prediction model was then conducted in this chapter. The primary

purpose of developing such a model is to provide structural engineers with a more accessible estimation tool to predict the internal overpressure-history curve with acceptable accuracy in the tunnel design phase. For engineering design practice, the main structure is supposed to maintain integrity in a gas explosion accident to constrain the accident's impact as much as possible, meaning the tunnel walls will not experience complete deformation. Hence, the tunnel cover was considered as a rigid wall with one vent opening at the opposite of the ignition end, and the inner obstacles were fixed to obtain a conservative load for design practice. The vent opening activation pressure, vent opening size, vent opening length, methane concentration, internal obstacles' height (blockage) and separation distance were considered in the proposed model. The schematic diagram of the tunnel for overpressure-history model development is shown in Fig. 25. A homogeneous methane-air mixture was filled in the tunnel with a length, height, and volume of $l$, d, and $V$, respectively. The ignition was placed at the center of one end of the tunnel while the vent opening was the opposite. The area, length, and activation pressure of the vent opening were $A_v$, $l_v$, and $p_v$, respectively. Obstacles were placed at the bottom of the tunnel with an identical separation distance of $\triangle l$ and had the same width as the tunnel. A set of 280 FLACS simulations were carried out to determine the critical parameters in the proposed model.
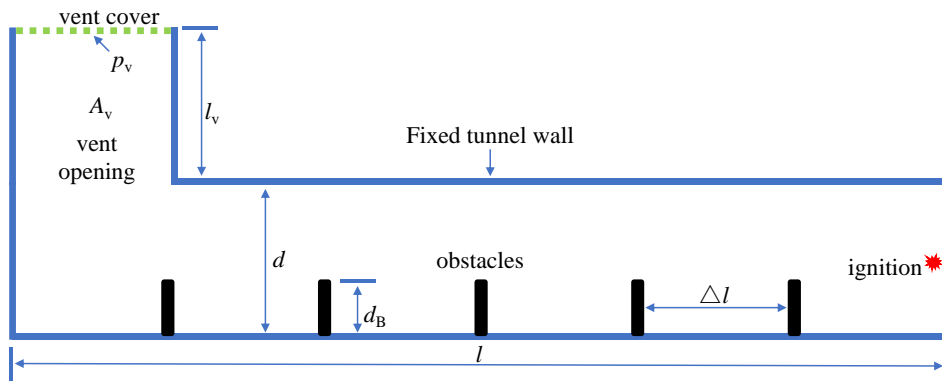


**Fig. 25.** Schematic diagram of the tunnel for overpressure-history model development

As illustrated in Fig. 26, the maximum peak impulse was observed at the ignition side, while the maximum peak pressure was on the opposite side. Therefore, it would represent the loads at the two sides of the tunnel for structural design, so the overpressure-history model mentioned above was aimed to predict the load profile at the two ends of the tunnel.
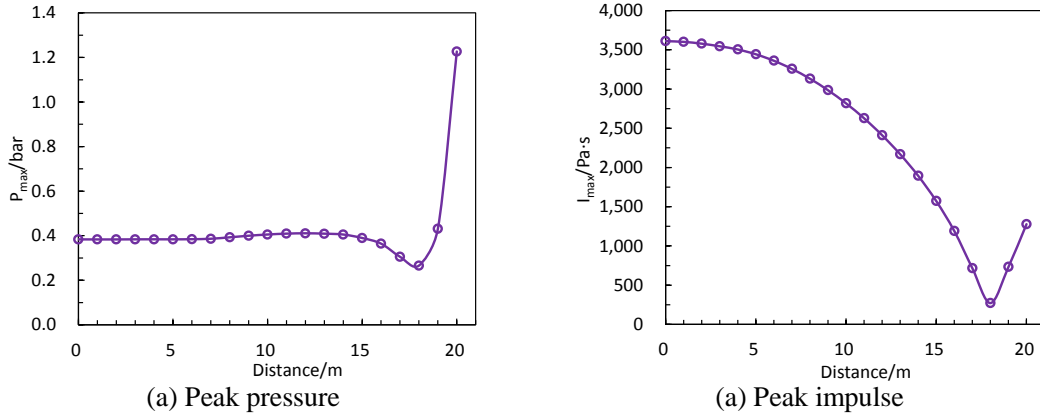
(a) Peak pressure          (a) Peak impulse

**Fig. 26.** The peak pressure and impulse distribution along the tunnel length

Furthermore, as illustrated in Fig. 27 (a) and (b), it was observed that the pressure profile had one dominant peak when $l_v=0$ m. By comparison, two prominent peaks were identified when $l_v=1.2$ m. The load curves were simplified, as shown in Fig. 27 (c) and (d). The overpressure history model predicted the value of pressure and time at characteristic points A, B, C, D, and E. It should be noted that at point B and the end of the curve, the overpressures were always 0.1 bar, as the pressure was usually accompanied by oscillation when the pressure was low.
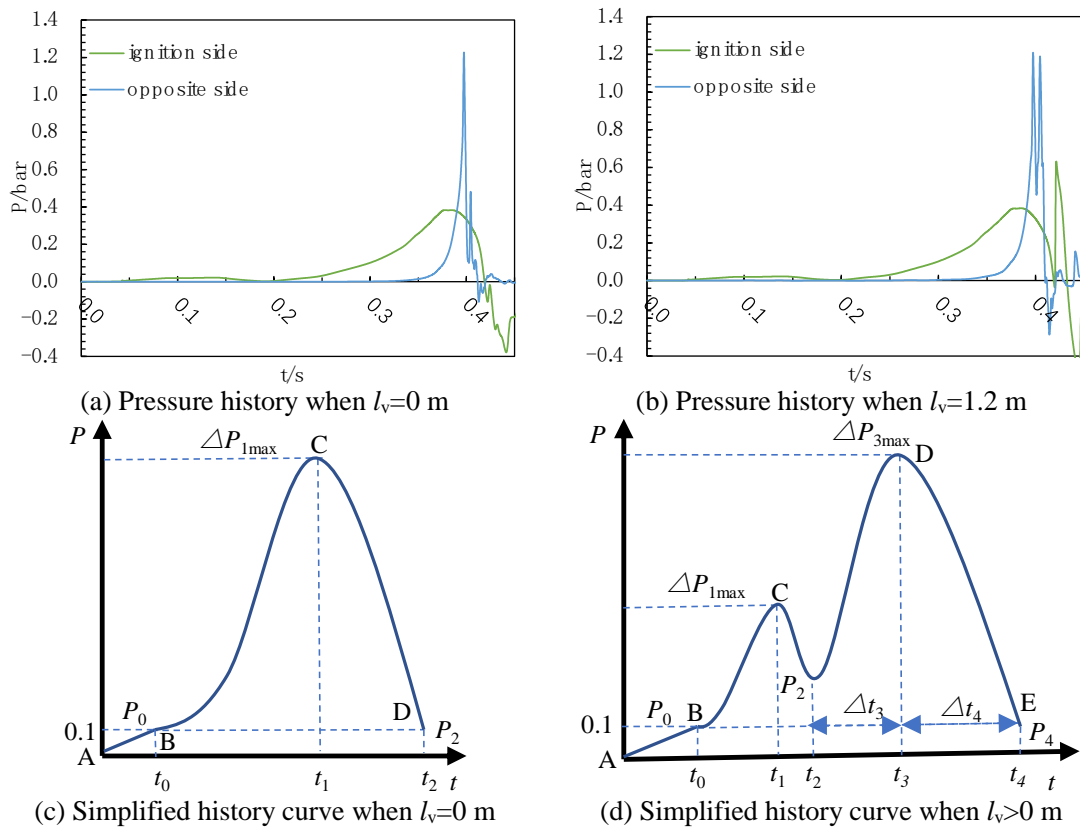


(a) Pressure history when $l_v=0$ m       (b) Pressure history when $l_v=1.2$ m

(c) Simplified history curve when $l_v=0$ m     (d) Simplified history curve when $l_v>0$ m

**Fig. 27.** Two typical pressure history profiles when $l_v=0$ m and $l_v>0$ m

Dimensionless variables were introduced in the overpressure history prediction model by referring to literature (Crescitelli et al., 1979; Li and Hao, 2019; Yang et al., 2021).

Specifically, dimensionless overpressure $\triangle p$ was defined as $\dfrac{p}{p_0}$, where $p$ and $p_0$ were the overpressure and atmospheric pressure in the unit of bar. Dimensionless vent cover activation pressure $p_\text{v} = \dfrac{p_\text{activation}}{p_0}$, vent coefficient $K_\text{v} = \dfrac{V^{2/3}}{A_\text{v}}$, dimensionless vent opening length $L_\text{v} = L/\sqrt{A_\text{v}}$, methane stoichiometric ratio $\phi$, blockage ratio $BR = \dfrac{d_\text{B}}{d}$, and dimensionless obstacle separation distance $L_\text{n} = \Delta l / l$ were used to represent the vent cover activation pressure, vent opening size, methane concentration, inner obstacles' height (blockage) and separation distance, respectively. Hence the objective prediction model can be expressed as $p(t) = f(p_\text{v}, \phi, K_\text{v}, BR, L_\text{n}, L_\text{v})$. According to the simulation results, the peak overpressure appeared to be a symmetric trend with the methane stoichiometric ratio, and reached its peak when $\phi = 1.1$; hence the form of formula $P = k_1 \times \mathrm{e}^{-k_2 \times (\phi - 1.1)^2}$ was used to fit the relationship between peak pressure and stoichiometric ratio. The relevant results can be found in Fig. 28.
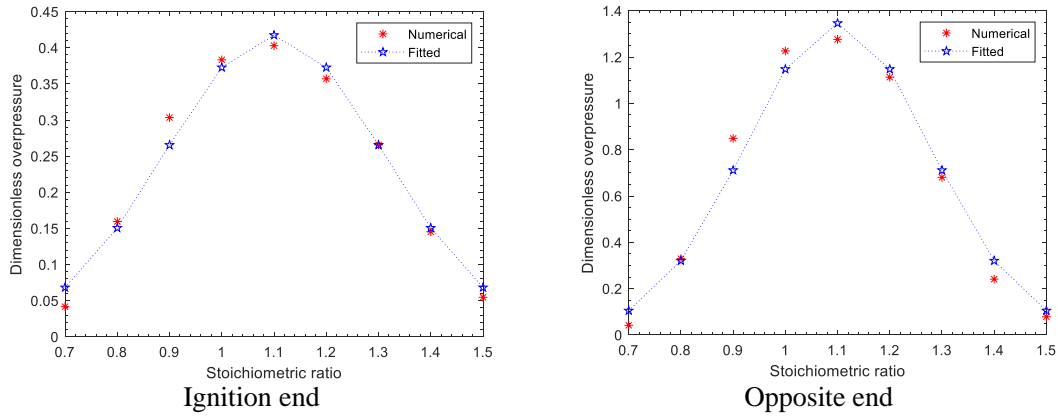


|                | |
|----------------|---|
| Ignition end   | Opposite end |

**Fig. 28.** The comparison of numerical and fitted peak pressure using the forms of
$$P = k_1 \times \mathrm{e}^{-k_2 \times (\phi - 1.1)^2}$$

It was found that the first peak pressure had a linear relationship with the vent cover activation pressure (Li et al., 2017; Yang et al., 2021), and the power function model was selected for nonlinear regression for the rest of the variables. The least squares method was used to fit for the characteristic points and variables, and the empirical formula at the ignition and opposite ends are shown in Eq. 1 and Eq. 2, respectively. The presented formula was developed through the 280 numerical simulations where the investigated tunnel length was from 10 to 30 m, the tunnel volumes varied from 9.6 to 32 m³, the activation pressure of the vent cover from 0 to 8 kPa (Li et al., 2019), the methane-air methane stoichiometric ratio was in the range of 0.8 to 1.4, the vent coefficient was from 1.8 to 7.5, the block ratio was less than 0.25 and the dimensionless vent opening length was from 0 to 1.25.
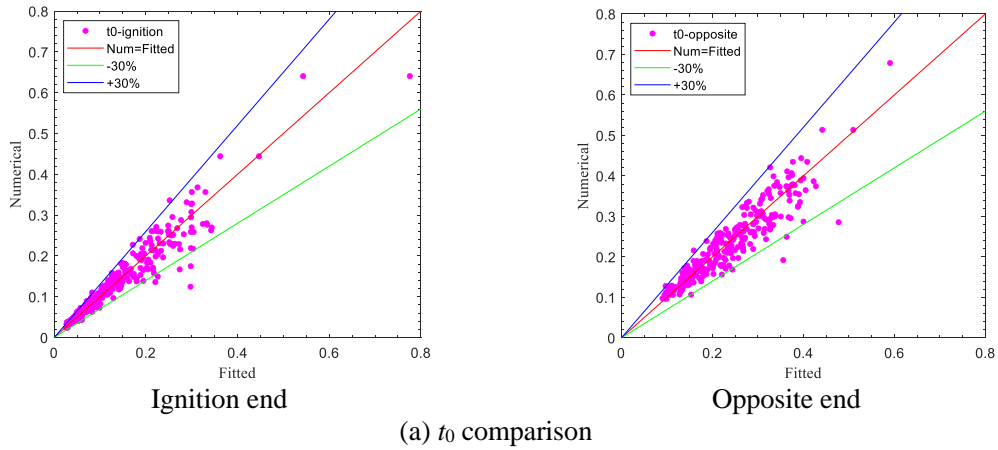
$$\begin{cases} t_{0\text{-ignition}} = -0.309\,p_v + e^{7.323\times(\phi-1.1)^2} \cdot \left(1+K_v\right)^{-0.97} \cdot \left(1+BR\right)^{-3.307} \cdot \left(1+L_n\right)^{-0.119} \cdot \left(1+L_v\right)^{-0.318}, \ p_0 = 0.1 \\[4pt] t_{1\text{-ignition}} = t_{0\text{-ignition}} + 1.132\,p_v + e^{-8.476\times(\phi-1.1)^2} \cdot \left(1+K_v\right)^{-1.726} \cdot \left(1+BR\right)^{-2.865} \cdot \left(1+L_n\right)^{-0.616} \cdot \left(1+L_v\right)^{-0.562}, \\[4pt] \Delta p_{1\max-\text{ignition}} = 0.348\,p_v + e^{-7.538\times(\phi-1.1)^2} \cdot \left(1+K_v\right)^{-0.349} \cdot \left(1+BR\right)^{10.168} \cdot \left(1+L_n\right)^{-0.846} \cdot \left(1+L_v\right)^{0.172} \\[4pt] t_{2\text{-ignition}} = t_{1\text{-ignition}} - 0.127\,p_v + e^{-4.408(\phi-1.1)^2} \cdot \left(1+K_v\right)^{-8.078} \cdot \left(1+BR\right)^{23.528} \cdot \left(1+L_n\right)^{7.635} \cdot \left(1+L_v\right)^{0.125}, \\[4pt] p_{2\text{-ignition}} = 0.1 \ (p_2 = 0 \ \text{if} \ L_v \neq 0) \\[4pt] \Delta t_3 = 3 \text{ ms}, \ \Delta p_{3\max-\text{ignition}} = 0.957\Delta p_{3\max-\text{opposite}} + \left(1+p_v\right)^{118.1} \cdot \left(1+L_v\right)^{-12.554} \\[4pt] \Delta t_{4\text{-ignition}} = 0.007\Delta p_{3\max\text{-ignition}} + 0.003, \ p_4 = 0.1 \end{cases}$$

$$(1)$$

$$\begin{cases} t_{0\text{-opposite}} = 0.492\,p_v + e^{5.563\times(\phi-1.1)^2} \cdot \left(1+K_v\right)^{-0.755} \cdot \left(1+BR\right)^{-2.915} \cdot \left(1+L_n\right)^{-0.135} \cdot \left(1+L_v\right)^{-0.308}, \ p_0 = 0.1 \\[4pt] t_{1\text{-opposite}} = t_{0\text{-opposite}} + 0.136\,p_v + e^{-8.148\times(\phi-1.1)^2} \cdot \left(1+K_v\right)^{0.756} \cdot \left(1+BR\right)^{-108.523} \cdot \left(1+L_n\right)^{-6.5} \cdot \left(1+L_v\right)^{0.016}, \\[4pt] \Delta p_{1\max\text{-opposite}} = 1.659\,p_v + e^{-10.281\times(\phi-1.1)^2} \cdot \left(1+K_v\right)^{-0.324} \cdot \left(1+BR\right)^{9.22} \cdot \left(1+L_n\right)^{0.813} \cdot \left(1+L_v\right)^{0.005} \\[4pt] t_{2\text{-opposite}} = t_{1\text{-opposite}} + 0.024\,p_v + e^{-9.485\times(\phi-1.1)^2} \cdot \left(1+K_v\right)^{1.365} \cdot \left(1+BR\right)^{-172.214} \cdot \left(1+L_n\right)^{-9.115} \cdot \left(1+L_v\right)^{-1.489}, \\[4pt] p_2 = 0.233\Delta p_{1\max\text{-opposite}} + \left(1+p_v\right)^{4.782} \cdot \left(1+L_v\right)^{-2.678} \\[4pt] \Delta t_3 = 3 \text{ ms}, \ \Delta p_{3\max-\text{opposite}} = -0.249\Delta p_{1\max-\text{opposite}} + \left(1+p_v\right)^{4.364} \cdot \left(1+L_v\right)^{0.511} \\[4pt] \Delta t_{4\text{-opposite}} = 0.004\Delta p_{3\max\text{-opposite}} + 0.003, \ p_4 = 0.1 \end{cases}$$
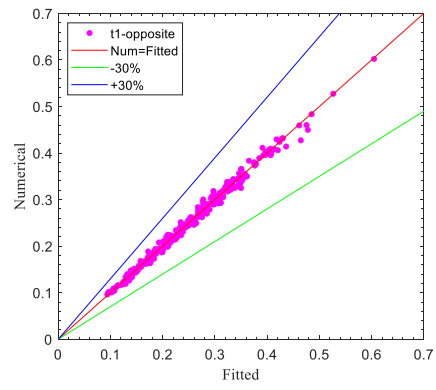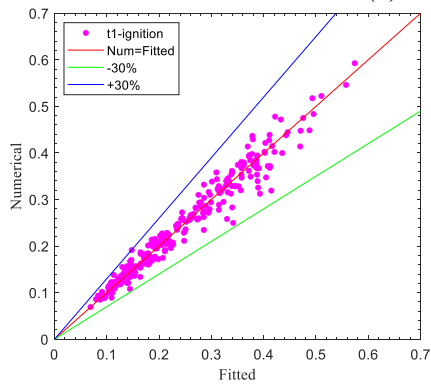
$$(2)$$

Fig. 29 presents a comparison between the fitted and numerical results. It can be seen that almost all the fitted peak pressure and the corresponding time fell in the deviation of $\pm$ 30%. Hence a reasonable accuracy was achieved.
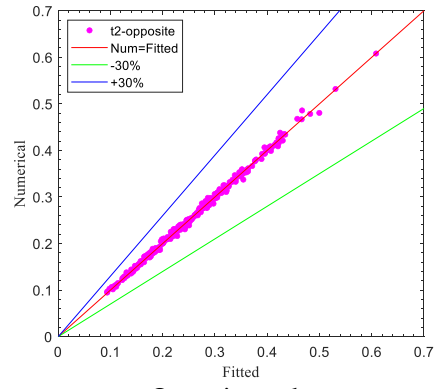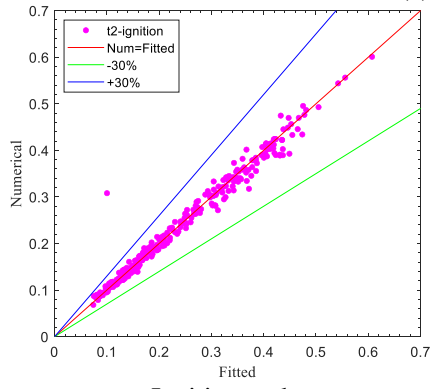


Ignition end          Opposite end

(a) $t_0$ comparison

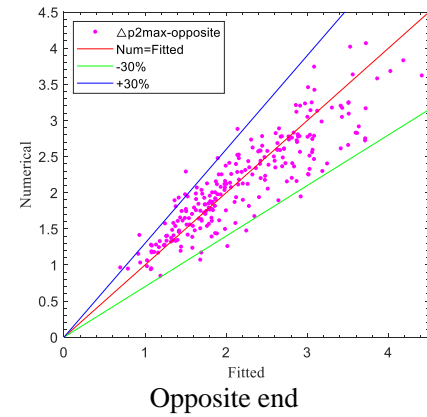Ignition end　　　　　　　　　Opposite end

(b) $\triangle p_{1max}$ comparison

Ignition end　　　　　　　　　Opposite end
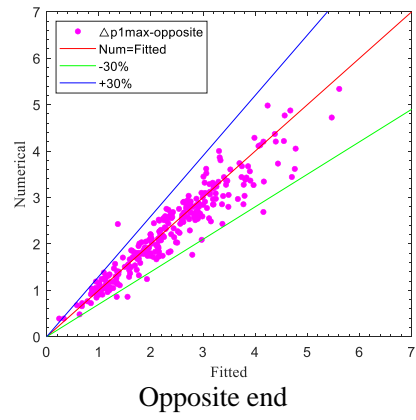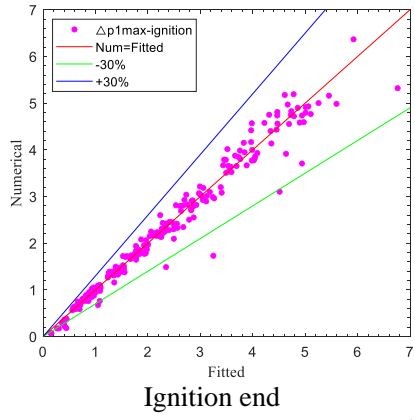
(c) $t_1$ comparison

Ignition end　　　　　　　　　Opposite end

(d) $t_2$ comparison

Ignition end　　　　　　　　　Opposite end

23

(e) $\triangle p_{2max}$ comparison
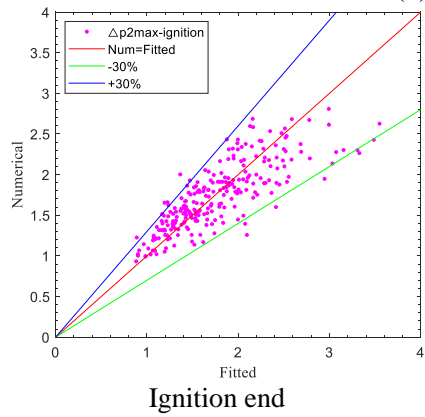


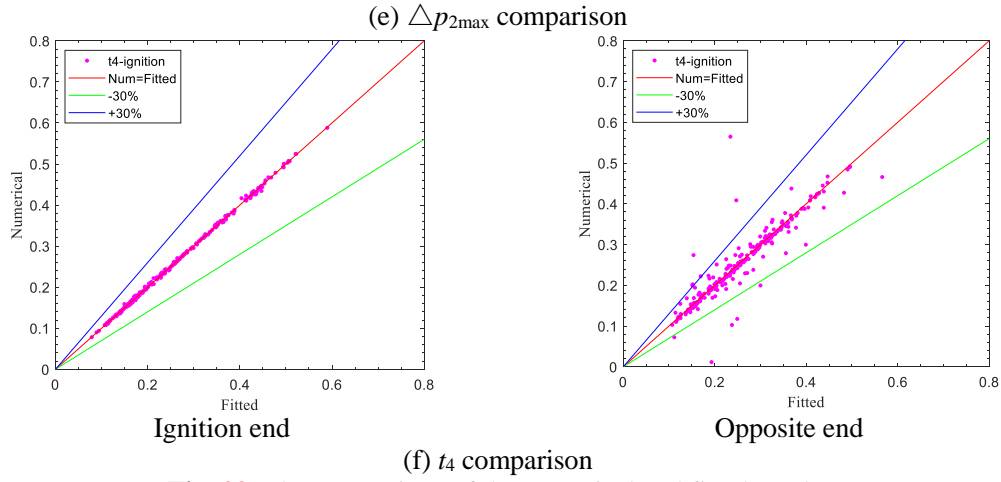| Ignition end | Opposite end |

(f) $t_4$ comparison

**Fig. 29.** The comparison of the numerical and fitted results

Even though the pressures and time at the characteristic point were predicted within acceptable accuracy, another challenge was to connect these scatter points smoothly and precisely. Generally, this was achieved by a specific interpolation algorithm. Here, the built-in function PCHIP based on the piecewise cubic Hermite interpolation algorithm in MATLAB® (Rabbath and Corriveau, 2019) was utilized to interpolate the overpressure between characteristic points for cases with *BR*=0. As shown in Eq. 3 and Eq. 4, to achieve a higher pressure growth rate caused by obstacles, the formula consisted of the power and exponential function were specially tuned to calculate the pressure value at the ignition side and opposite side when the time was between $t_1$ and $t_2$ if $BR \neq 0$. As illustrated in Fig. 30, the pressure in Figures (a) and (b) was interpolated by Eq. 3 and Eq. 4, while those in Figures (c) and (d) were interpolated using the PCHIP function. The pressure-time history showed a smooth transition between characteristic points, and the main features of the increasing and decreasing trend can be captured by combining the presented empirical formula and interpolation algorithm.

$$P = \begin{cases} P_0 + A(1 + e^{-(\varphi-1.1)^2})^{200 \cdot BR \cdot t}, & t_{0\text{-ignition}} < t < t_{1\text{-ignition}} \\ \Delta p_{1max-\text{ignition}} - \left[ P_0' + B(1 + e^{-(\varphi-1.1)^2})^{250 \cdot BR \cdot (t_{2\text{-ignition}} - t)} \right], & t_{1\text{-ignition}} < t < t_{2\text{-ignition}} \end{cases} \quad (3)$$

$$P = \begin{cases} P_0 + A(1 + e^{-(\varphi-1.1)^2})^{5000 \cdot BR \cdot t}, & t_{0\text{-opposite}} < t < t_{1\text{-opposite}} \\ \Delta p_{1max-\text{opposite}} - \left[ P_0' + B(1 + e^{-(\varphi-1.1)^2})^{5000 \cdot BR \cdot (t_{2\text{-opposite}} - t)} \right], & t_{1\text{-opposite}} < t < t_{2\text{-opposite}} \end{cases} \quad (4)$$

(a) Ignition end with a single prominent peak



(b) Opposite end with a single prominent peak



(c) Ignition end with two prominent peaks



(d) Opposite end with two prominent peaks

**Fig. 30.** The comparison of the interpolation-based and numerical history curve, (a) and (b) were based on Eq. 3 and Eq. 4, and (c) and (d) were based on cubic Hermite interpolation algorithm
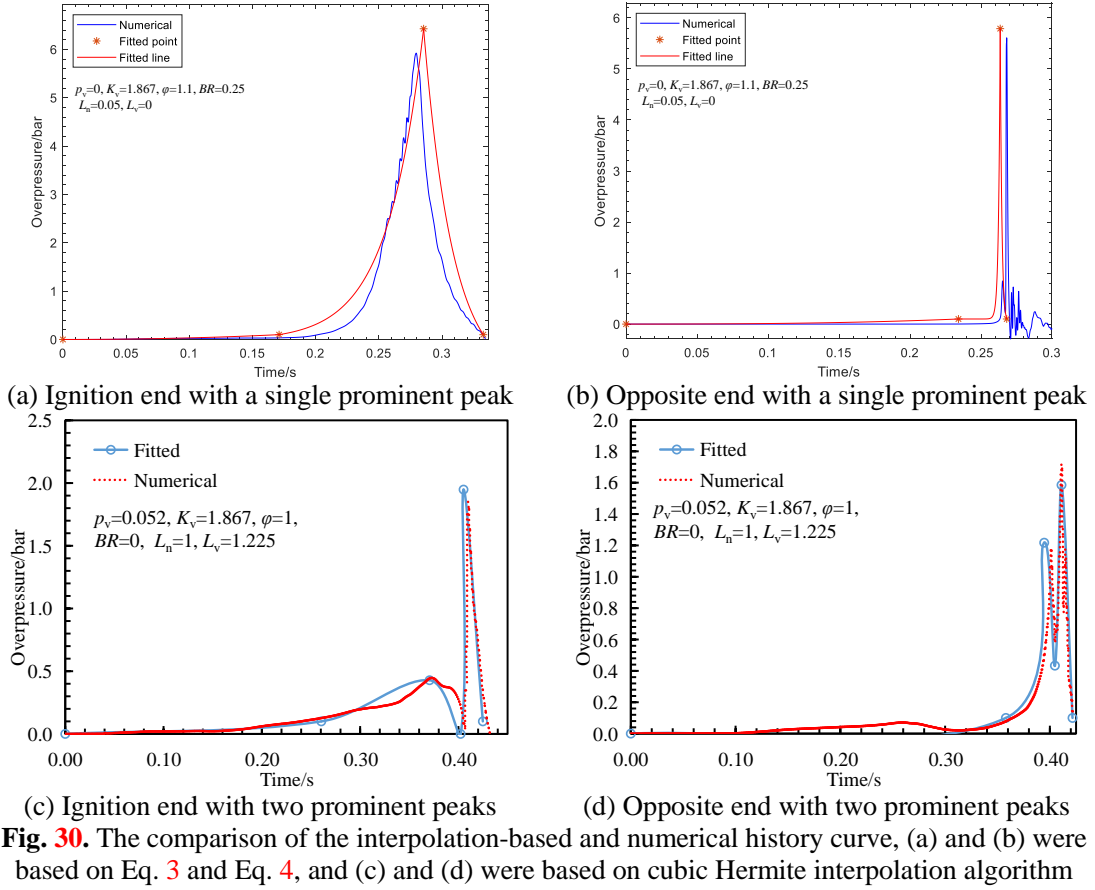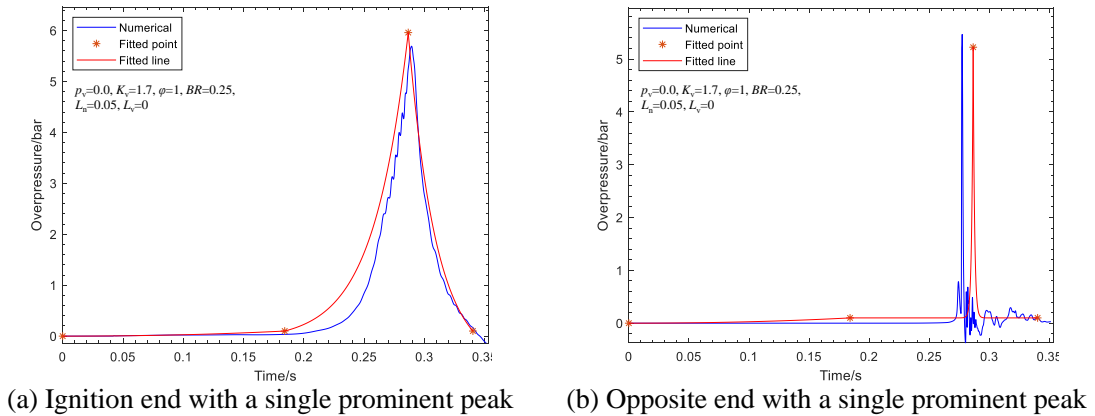
Fig. 31 depicts two new simulations not contained in the fitting dataset to validate the proposed model further. Again, the main characteristics were predicted by the proposed model with acceptable accuracy.
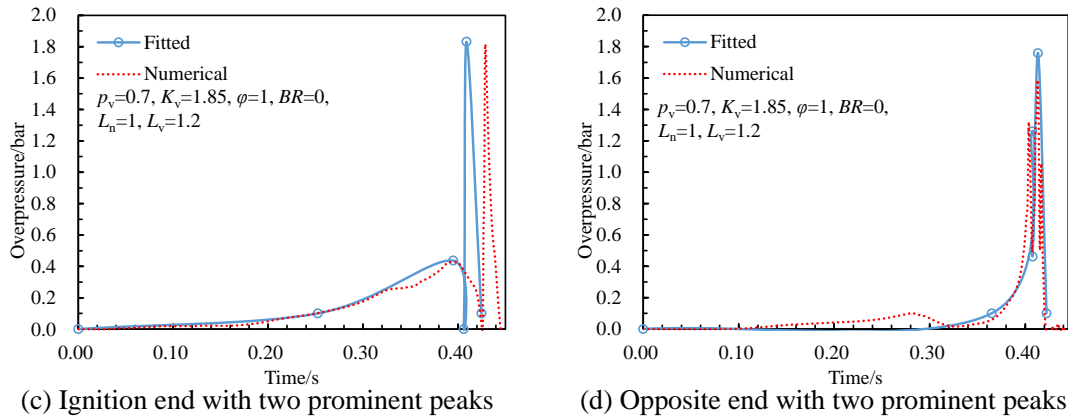


(a) Ignition end with a single prominent peak



(b) Opposite end with a single prominent peak

(c) Ignition end with two prominent peaks     (d) Opposite end with two prominent peaks

**Fig. 31.** The comparison of the presented model and numerical history curve

## 5 Conclusions

A parametric study of methane-air explosion in tunnel-shape space was performed to study the effect of tunnel's boundary conditions on overpressure and impulse using the CFD tool FLACS. An overpressure-history prediction model was also proposed and validated based on simulation results.

As the activation pressure of tunnel cover rose but less than 6 bar, the inner peak pressure increased and the tunnel cover was damaged progressively. By comparison, the inner peak pressure maintained steady and the tunnel cover kept its integrity as the activation pressure of tunnel cover reached 8 bar or higher. Wider single piece of tunnel cover panel had no notable influence on the peak overpressure but reduced pressure duration and impulse significantly. Longer tunnel led to increase in both peak pressure and impulse, while for the fixed tunnel length cases, closer obstacles or higher activation pressure of obstacles contributed to higher peak pressure but reduced impulse. A local expansion far away from the ignition point enhanced the peak pressure significantly.

280 numerical results were utilized to develop two categories of equations considering activation pressure of vent cover area and length of vent opening, methane concentration, blockage ratio caused by the inner obstacle, and obstacles' distance to calculate the overpressure and corresponding time at the characteristic points of the pressure history curve. The cubic Hermite interpolation algorithm was accurate enough to interpolate the pressure value between characteristic points when there are no obstacles inside the tunnel. Meanwhile, another specially tuned formula consisting of the power and exponential function was used to calculate the pressure value between the second and fourth characteristic points for the tunnel with inner obstacles. The proposed model can predict both the peak pressure and the overpressure history with acceptable accuracy.

26

**References**

National Fire Protection Association, 2023. Standard on Explosion Protection by Deflagration Venting. https://link.nfpa.org/free-access/publications/68/2023.

Bjerketvedt, D., Bakke, J.R., van Wingerden, K., 1997. Gas explosion handbook. J. Hazard. Mater. 52, 1-150, http://doi.org/10.1016/S0304-3894(97)81620-2.

BP, P.L.C., 2022. Statistical Review of World Energy. http://doi.org/https://www.bp.com/content/dam/bp/business-sites/en/global/corporate/pdfs/energy-economics/statistical-review/bp-stats-review-2022-full-report.pdf.

Bradley, D., Mitcheson, A., 1978a. The Venting of Gaseous Explosions in Spherical Vessels. l-Theory. Combust. Flame 221-236, http://doi.org/10.1016/0010-2180(78)90098-6.

Bradley, D., Mitcheson, A., 1978b. The Venting of Gaseous Explosions in Spherical Vessels. ll-Theory and Experiment. Combust. Flame 32, 237-255, http://doi.org/10.1016/0010-2180(78)90099-8.

Canu, P., Rota, R., Carrà, S., Morbidelli, M., 1990. Vented gas deflagrations a detailed mathematical model tuned on a large set of experimental data. Combust. Flame 80, 49-64, http://doi.org/https://doi.org/10.1016/0010-2180(90)90051-R.

Chen, C., Li, C., Reniers, G., Yang, F., 2021. Safety and security of oil and gas pipeline transportation: A systematic analysis of research trends and future needs using WoS. J. Clean Prod. 279, 123583, http://doi.org/10.1016/j.jclepro.2020.123583.

Chen, D., Wu, C., Li, J., Liao, K., 2022. A numerical study of gas explosion with progressive venting in a utility tunnel. Process Saf. Environ. Protect. 162, 1124-1138, http://doi.org/10.1016/j.psep.2022.05.009.

Chippett, S., 1984. Modeling of vented deflagrations. Combust. Flame 55, 127-140, http://doi.org/https://doi.org/10.1016/0010-2180(84)90022-1.

Crescitelli, S., Russo, G., Tufano, V., 1979. Analysis and design of venting systems: A simplified approach. Journal of Occupational Accidents 2, 125-133, http://doi.org/https://doi.org/10.1016/0376-6349(79)90004-X.

Ministry of Housing and Development, 2015. Technical code for urban utility tunnel engineering. 1-104.

Feldgun, V.R., Karinski, Y.S., Yankelevsky, D.Z., 2011. A simplified model with lumped parameters for explosion venting simulation. Int. J. Impact Eng. 38, 964-975, http://doi.org/10.1016/j.ijimpeng.2011.08.004.

Gexcon, 2019. FLACS v10.9 User's Manual.

Hou, L., Li, Y., Qian, X., Shu, C., Yuan, M., Duanmu, W., 2021. Large-scale experimental investigation of the effects of gas explosions in underdrains. Journal of Safety Science and Resilience 2, 90-99, http://doi.org/10.1016/j.jnlssr.2021.03.001.

Hu, Q., Zhang, Q., Yuan, M., Qian, X., Li, M., Wu, H., Shen, X., Liang, Y., 2022. Traceability and failure consequences of natural gas explosion accidents based on key investigation technology. Eng. Fail. Anal. 139, 106448, http://doi.org/10.1016/j.engfailanal.2022.106448.

Li, J., Hao, H., 2019. Numerical and analytical prediction of pressure and impulse from vented gas explosion in large cylindrical tanks. Process Saf. Environ. Protect. 127, 226-244, http://doi.org/10.1016/j.psep.2019.05.019.

Li, J., Hernandez, F., Hao, H., Fang, Q., Xiang, H., Li, Z., Zhang, X., Chen, L., 2017. Vented Methane-air Explosion Overpressure Calculation—A simplified approach based on CFD. Process Saf. Environ. Protect. 109, 489-508, http://doi.org/10.1016/j.psep.2017.04.025.

Li, P., Huang, P., Liu, Z., Du, B., Li, M., 2019. Experimental study on vented explosion overpressure of methane/air mixtures in manhole. J. Hazard. Mater. 374, 349-355, http://doi.org/10.1016/j.jhazmat.2019.04.046.

Li, Z., Chen, L., Fang, Q., Hao, H., Zhang, Y., Xiang, H., Chen, W., Yang, S., Bao, Q., 2017. Experimental and numerical study of unreinforced clay brick masonry walls subjected to vented gas explosions. Int. J. Impact Eng. 104, 107-126, http://doi.org/10.1016/j.ijimpeng.2017.02.002.

Li, Z., Chen, L., Yan, H., Fang, Q., Zhang, Y., Xiang, H., Liu, Y., Wang, S., 2021. Gas explosions of methane-air mixtures in a large-scale tube. Fuel 285, 119239, http://doi.org/10.1016/j.fuel.2020.119239.

Li, Z., Wu, J., Liu, M., Li, Y., Ma, Q., 2020. Numerical Analysis of the Characteristics of Gas Explosion Process in Natural Gas Compartment of Utility Tunnel Using FLACS. Sustainability 12, 153, http://doi.org/10.3390/su12010153.

Liao, K., Wang, Y., Chen, D., He, G., Huang, Y., Zhang, S., Qin, M., He, T., 2023. Parametric Study on Natural Gas Leakage and Diffusion in Tunnels. J. Pipel. Syst. Eng. Pract. 14, http://doi.org/10.1061/JPSEA2.PSENG-1396.

Lin, S., Hou, Q., Derlatka, A., Gao, S., Kang, J., Dong, X., 2022. The Study on the Shock Wave Propagation Rule of a Gas Explosion in a Gas Compartment. Shock Vib. 2022, 1-17, http://doi.org/10.1155/2022/5938950.

Lin, Z., Guo, C., Ni, P., Cao, D., Huang, L., Guo, Z., Dong, P., 2020. Experimental and numerical investigations into leakage behaviour of a novel prefabricated utility tunnel. Tunn. Undergr. Space Technol. 104, 103529, http://doi.org/10.1016/j.tust.2020.103529.

Meng, Q., Wu, C., Hao, H., Li, J., Wu, P., Yang, Y., Wang, Z., 2020a. Steel fibre reinforced alkali-activated geopolymer concrete slabs subjected to natural gas explosion in buried utility tunnel. Constr. Build. Mater. 246, 118447, http://doi.org/10.1016/j.conbuildmat.2020.118447.

Meng, Q., Wu, C., Li, J., Liu, Z., Wu, P., Yang, Y., Wang, Z., 2020b. Steel/basalt rebar reinforced Ultra-High Performance Concrete components against methane-air explosion loads. Composites Part B: Engineering 198, 108215, http://doi.org/10.1016/j.compositesb.2020.108215.

Meng, Q., Wu, C., Li, J., Wu, P., Xu, S., Wang, Z., 2021. A study of pressure characteristics of methane explosion in a 20 m buried tunnel and influence on structural behaviour of concrete elements. Eng. Fail. Anal. 122, 105273, http://doi.org/10.1016/j.engfailanal.2021.105273.

Puttock, J.S., Yardley, M.R., Cresswell, T.M., 2000. Prediction of vapour cloud explosions using the SCOPE model. J. Loss Prev. Process Ind. 13, 419-431, http://doi.org/https://doi.org/10.1016/S0950-4230(99)00045-5.

European Committee for Standardization., 2007. Gas Explosion Venting Protective Systems.

Yang, H., Chen, J., Chiu, H., Kao, T., Tsai, H., Chen, J., 2016. Confined vapor explosion in Kaohsiung City – A detailed analysis of the tragedy in the harbor city. J. Loss Prev. Process Ind. 41, 107-120, http://doi.org/10.1016/j.jlp.2016.03.017.

Yang, S., Cai, J., Yang, Y., Fang, Q., Bao, Q., Wang, S., 2021. Investigation of a semi-empirical load model of natural gas explosion in vented spaces. Journal of Safety Science and Resilience 2, 157-171, http://doi.org/10.1016/j.jnlssr.2021.08.008.

Yang, Y., Yang, S., Fang, Q., Xiang, H., Sun, W., Liu, X., 2022. Large-scale experimental and simulation study on gas explosion venting load characteristics of urban shallow buried pipe trenches. Tunn. Undergr. Space Technol. 123, 104409, http://doi.org/10.1016/j.tust.2022.104409.

Zhang, S., Ma, H., Huang, X., Peng, S., 2020. Numerical simulation on methane-hydrogen explosion in gas compartment in utility tunnel. Process Saf. Environ. Protect. 140, 100-110, http://doi.org/10.1016/j.psep.2020.04.025.

Zhao, Y., Wu, J., Zhou, R., Cai, J., Bai, Y., Pang, L., 2022. Effects of the length and pressure relief conditions on propagation characteristics of natural gas explosion in utility tunnels. J. Loss Prev. Process Ind. 75, 104679, http://doi.org/10.1016/j.jlp.2021.104679.

Zhu, Y., Qian, X., Liu, Z., Huang, P., Yuan, M., 2015. Analysis and assessment of the Qingdao crude oil vapor explosion accident: Lessons learnt. J. Loss Prev. Process Ind. 33, 289-303, http://doi.org/10.1016/j.jlp.2015.01.004.

Zhu, Y., Wang, D., Shao, Z., Xu, C., Li, M., Zhang, Y., 2021. Characteristics of methane-air explosions in large-scale tunnels with different structures. Tunn. Undergr. Space Technol. 109, 103767, http://doi.org/10.1016/j.tust.2020.103767.

Zhu, Y., Wang, D., Shao, Z., Zhu, X., Xu, C., Zhang, Y., 2020. Investigation on the overpressure of methane-air mixture gas explosions in straight large-scale tunnels. Process Saf. Environ. Protect. 135, 101-112, http://doi.org/10.1016/j.psep.2019.12.022.

Zipf, R.K., Gamezo, V.N., Sapko, M.J., Marchewka, W.P., Mohamed, K.M., Oran, E.S., Kessler, D.A., Weiss, E.S., Addis, J.D., Karnack, F.A., Sellers, D.D., 2013. Methane–air detonation experiments at NIOSH Lake Lynn Laboratory. J. Loss Prev. Process Ind. 26, 295-301, http://doi.org/10.1016/j.jlp.2011.05.003.